Experimental Assessment of Real-Time Brain Stroke Monitoring via a Microwave Imaging Scanner

DAVID O. RODRIGUEZ-DUARTE[1] **(Graduate Student Member, IEEE), CRISTINA ORIGLIA**[1] **,**
JORGE A. TOBÓN VASQUEZ[1] **(Member, IEEE), ROSA SCAPATICCI**[2] **(Member, IEEE),**
LORENZO CROCCO[2] **(Senior Member, IEEE), AND FRANCESCA VIPIANA**[1] **(Senior Member, IEEE)**

[1]Department of Electronics and Telecommunications, Politecnico di Torino, 10129 Turin, Italy

[2]Institute for the Electromagnetic Sensing of the Environment, National Research Council of Italy, 80124 Naples, Italy

CORRESPONDING AUTHORS: D. O. RODRIGUEZ-DUARTE AND F. VIPIANA (e-mail: david.rodriguez@polito.it; francesca.vipiana@polito.it)

ABSTRACT This paper presents the experimental validation of a microwave imaging system for real-time monitoring of brain stroke in the post-acute stage. The system exploits a low-complexity sensing apparatus and a multi-frequency microwave imaging algorithm with a novel artifact removal feature. Phantoms of a homogeneous anthropomorphic head and an ellipsoidal non-static stroke mimicking target, varying gradually from $0\,cm^3$ to $60\,cm^3$, are employed for the experiments. The phantom and the evolving target are filled with appropriate alcohol-based mixtures to mimic the different dielectric properties of the relevant tissue. The microwave imaging scanner operates using a 22-antennas architecture formed by printed flexible antennas with a custom-made matching medium. The system provides 3-D images of the entire brain region, exploiting differential multi-view scattering measures and the distorted Born approximation to build a pre-computed imaging kernel. The results show the system's capability to follow up the continuous progression of hemorrhage and ischemia zones with centimetric spatial resolution and to provide information on whether the stroke is growing or shrinking.

INDEX TERMS Biomedical electromagnetic imaging, brain stroke monitoring, distorted born approximation, flexible antennas, hemorrhagic stroke, ischemic stroke, inverse scattering, microwave antenna array, microwave imaging, microwave propagation.

I. INTRODUCTION

BRAIN stroke is a leading cause of death and disability worldwide and its incidence is expected to increase in the coming years due to rising average age and widespread risk factors, such as an unhealthy lifestyle [1]. Clinically, a stroke occurs when an artery to the brain clots or bursts; the first case is referred to as an ischemic (IS) stroke, and it accounts for nearly 85% of all strokes, while the remaining cases have hemorrhagic (HEM) nature, and they are often deadlier [2].

For either type, a continuous post-acute brain monitoring would provide clinicians a vital instrument to assess the effectiveness of administered therapies, thus, leading prompt and tailored actions. However, the current gold-standards image-based techniques, i.e., magnetic resonance (MRI) and

computed tomography (CT) lack real-time continuous monitoring capability, that limits the information about the stroke status during the post-acute phase, which is thus an unmet essential medical need.

In this context, microwave imaging (MWI) is a technology owing to short acquisition times, easy and safe deployment, cost-effectiveness, and portability, which enables bedside use and continuous follow-up [3], [4], relying on the perturbation of an excited electromagnetic (EM) field caused by the temporal variation of different dielectric properties of the stroke-affected tissue. Thus, MWI has potential significance for clinical practice since it can provide fast and continuous image outcomes with relevant information, albeit limited in resolution in comparison to MRI and CT.

Several MWI solutions have been developed, aiming to address the diagnosis and follow-up stroke, i.e., detection, identification, localization, and monitoring of the stroke-affected zone. [5] presents a multi-step learning-by-examples strategy to monitor stroke location and discriminate the typology in real-time, while [6] processes scattering data from a low-complexity system with a machine-learning algorithm, that allows stroke detection and classification in pre-clinical trials; though, both these examples do not provide the user with an image. Other systems exploit tomographic techniques to reconstruct an image of the brain and localize the unhealthy area [7]–[10]. Reference [7] employs a ring array of 8 antennas submerged in a liquid matching medium of glycerin to validate an iterative imaging algorithm able to quantitatively reconstruct the dielectric properties within the imaging domain, with the limit of higher execution time, thus, not real-time performance. References [8], [9] introduce a system composed of an antenna array ring with 16 cavity-backed elements working in a multi-view scheme. Reference [8] uses an adaptive Lebesgue-space based inversion algorithm, while [9] upgrades the imaging by developing a hybrid algorithm combining a fast qualitative process output with an accurate non-linear inversion. Both [8] and [9] provided 2-D experimental validation using cylindrical phantoms and 3-D numerical one employing anthropomorphic cases. [10], now EMTensor, realizes a high-complexity 3-D brain scanner with 177 probes fixed in 8 rings around a spherical cap that retrieves tomographic images to monitor the pathology, entailing long reconstruction times even using parallel computing [11]. Moreover, different imaging strategies provide fast qualitative reconstructions, focusing on stroke detection and localization [12]–[14]. Reference [12] presents an algorithm based on unsupervised machine learning exploiting the head symmetry and using a 14-element array tested on a multilayer phantom in hemorrhage-simulating scenarios. Reference [13] tests a confocal multistatic beamforming in a 2-D configuration, while in [14] the beamforming and polar sensitivity encoding (PSE) algorithms are applied in 3-D brain imaging. In this broad research context, it is evident that achieving stroke monitoring through real-time 3-D imaging, with the constraint of a low-complexity device, is still an open issue.

Furthermore, [15]–[17] present real-time MWI applied to other medical issues. Reference [15] integrates Born and Rytov linear approximations with quantitative microwave holography, allowing leverage of their advantages depending on the object's geometry and contrast. It experimentally tests the technique in a simplified breast imaging case. Finally, [16], [17] are examples of thermal monitoring, where real-time imaging is accomplished with a precomputed linear inverse scattering solution combined with scattering measurements. Summing up, MWI generally represents a good candidate for real-time imaging applications.

This contribution experimentally demonstrates for the first time, to the best of our knowledge, the use of MWI for continuous real-time follow-up of both HEM and IS post-acute
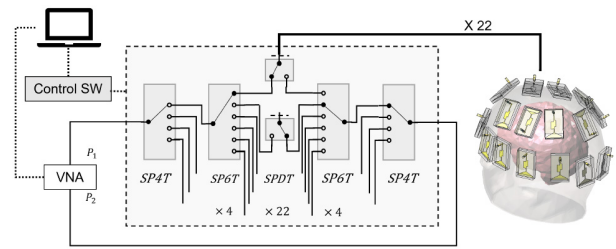

FIGURE 1. Hardware architecture of the brain stroke scanner prototype. The signal generated through a 2-port VNA is multiplexed via a switching matrix with 22 output ports connected to the antennas in the array. A laptop controls the switches and the VNA.

progressive evolution, localizing, and 3-D shape-retrieving the transition. To this end, starting from the switching mechanism in [18], a new optimized, compact, low-complexity radiating part of the MWI prototype is developed following the same rigorous design procedures in [19]. The prototype system consists of 22 compact and flexible antennas with custom matching mediums, collecting the multi-static multi-view scattering matrix. Moreover, unlike the previous works of the authors, where a single-frequency approach is used, here, it is employed a multifrequency imaging algorithm, providing information in a frequency band between 0.8 and 1 GHz, combined with an artifacts reduction procedure dealing with the distortions generated by noise propagation into the imaging kernel. The algorithm also includes an innovative procedure based on the sign of the retrieved dielectric contrast that indicates the recovery or worsening of the stroke-affected tissues. A preliminary analysis of the MWI scanner was recently presented in [20].

The paper is organized as follows. Section II describes the MWI system, detailing the antenna realization. Section III discusses the imaging algorithm and the adopted artifact removal procedure. Section IV presents the phantoms' realization and outlines the experimental procedure and the results. Finally, in Section V, the conclusion and the discussion of future perspectives are presented.

II. MICROWAVE IMAGING SYSTEM
A. BRAIN STROKE MONITORING SCANNER PROTOTYPE
The overall scheme of the brain stroke scanner is depicted in Fig. 1. A compact 2-port Vector Network Analyzer (VNA), P9375A Keysight Streamline USB VNA [21], provides the stimulus to the radiating unit and receives the response. The signal is efficiently multiplexed to a 22 antenna array through a switching matrix, allowing the acquisition of the complete scattering matrix. The switching matrix is realized by combining single-pole-four-throw (SP4T), single-pole-six-throw (SP6T), and single-pole-double-throw (SPDT) electromechanical coaxial switches interconnected with rigid coaxial cables [22]. The connections between the VNA, the switching matrix, and the antenna ports are realized with flexible coaxial cables. Finally, a laptop controls the switches collecting and processing the data and presenting the resulted images.

TABLE 1. Materials composition and target dielectric parameters at 1 GHz.

	Ingredients (% in weight)			Dielectric parameters	
	Water	90% Alcohol	Salt	ϵ_r	σ [S/m]
Brain	39.9	59.7	0.4	45	0.8
Hem	66.4	33	0.6	63	1.5
Isc	29.4	70.1	0.5	36	0.7
	Graphite	Rubber	–	ϵ_r	σ [S/m]
Matching	25	75		13	0.2
Substrate	35	65		18	0.3

To ensure an optimal trade-off between signal-to-noise ratio and measurement time, the VNA was set with an input power of 0 dBm and the intermediate filter (IF) to 100 Hz, allowing the collection of the complete scattering matrix for 5 frequency points in about 5 minutes. It is worth noticing that the measuring time is mainly dictated by the mechanical switching time in the multiplexing matrix.

B. MICROWAVE FLEXIBLE ANTENNA

The antenna array is arranged conformal to the upper part of the head as shown in Fig. 1. It is a novel version of the one used in the first generation device [23], in which the radiating element has been redesigned, reducing its the overall size and using flexible materials to improve the contact with the skin (see Fig. 2(a)). Each element has a dimension of 48 mm × 30 mm, with a thickness of around 10 mm, and is back-fed via a coaxial connector. The antenna comprises a ground (GND) plane, a triangular radiator and a feeding line, all printed on flexible commercial polyimide film (50 μm thick). A flexible dielectric substrate, with thickness of 5 mm, is placed between the radiator and the GND, and another one is the matching layer between the antenna and the head skin, as shown in Fig. 2(b). Both the antenna substrate and the matching layer are realized with custom mixtures of urethane rubber and graphite powder (i.e., G35 and G25, having 35 % and 25 % by volume of graphite, respectively) to achieve the desired permittivity and minimize losses. The percentage components in the materials and their dielectric characteristics at 1 GHz are summarized in Table 1.
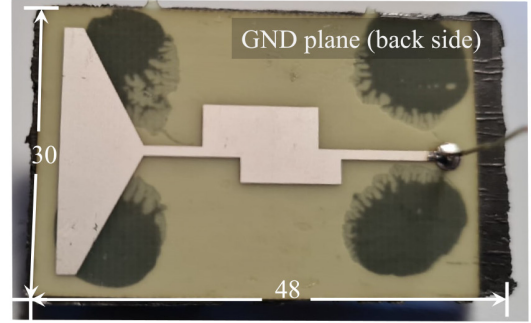
The reflection coefficients of the antennas are plotted in Fig. 2(c), where the antennas were placed on the phantom head (detailed in Section IV). Due to the unavoidable manufacturing errors, each antenna shows different behavior, especially in the proximity of the resonance. To minimize the impact of this variability on the imaging procedure and results, the frequency band between 0.8 and 1 GHz is selected to acquire the data, since this band provides manufacturing stability, and a good trade-off between penetration depth and resolution capability in brain imaging applications [19].

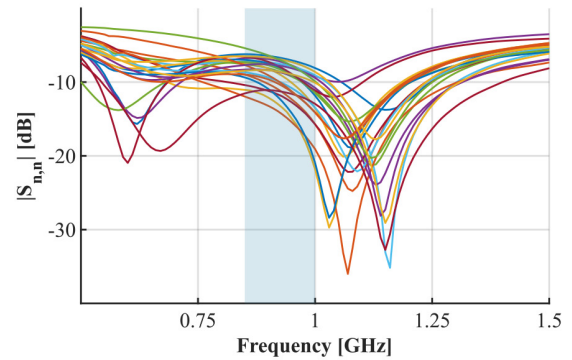## III. REAL-TIME MONITORING ALGORITHM

The developed monitoring algorithm aims for an imaging-based follow-up of a brain stroke condition in almost real-time, retrieving a complex contrast 3-D mapping while using input multi-frequency differential scattering parameters, collected in a multi-view scheme. The algorithm both reveals
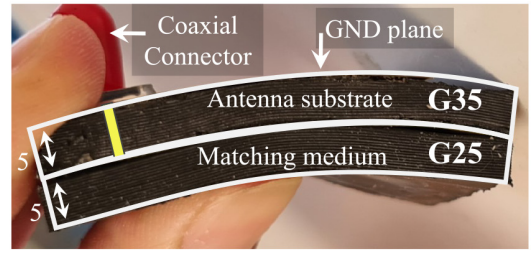
(a)

(b)

(c)

FIGURE 2. The antenna element. (a) Lateral view with the G35 substrate and G25 matching medium layer stacked; (b) top view. All dimensions are given in mm. (c) Reflection coefficients amplitude; each line corresponds to the n-th antenna of the MWI system, with n = 1, ..., 22.

the presence of a change in the stroke and indicates if the stroke is growing or shrinking. The algorithm scheme is illustrated in Fig. 3, and detailed in the following.

A. MATHEMATICAL MODEL

To monitor the time evolution of the stroke, a differential imaging scheme is adopted. In such an approach, the target of the imaging is represented by the spatial distribution of the variation of the electric contrast within the head between t_0 and t_1:

$$\Delta\chi(t_0, t_1) = \frac{\epsilon(t_1) - \epsilon(t_0)}{\epsilon_b}, \tag{1}$$

where $\epsilon(t_n)$ is the complex permittivity distribution at the time instant t_n, $n = 0, 1$, and b indicates a reference background scenario.

Since we face a monitoring scenario here, the dimension of the stroke variation can be assumed to be small, considering
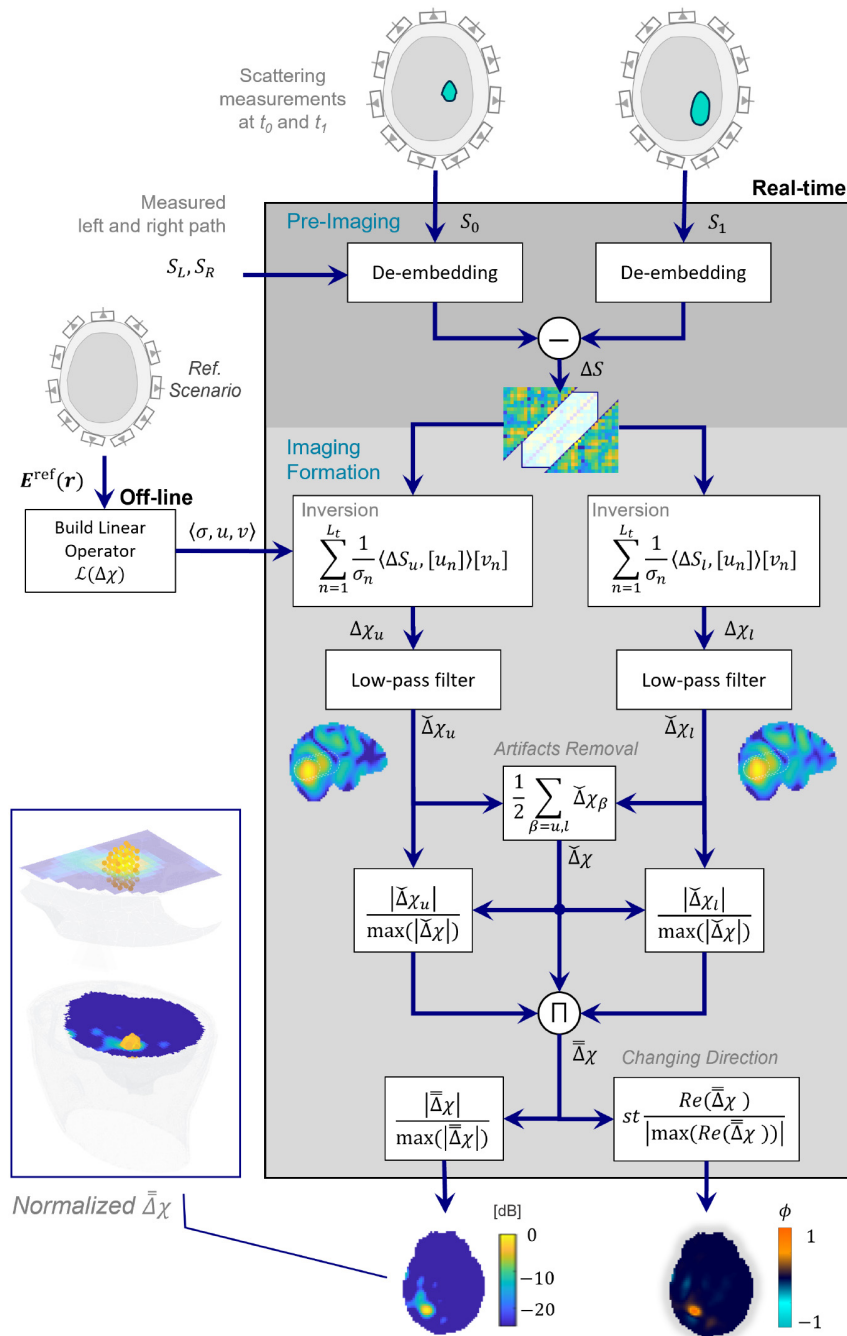
FIGURE 3. Scheme of the imaging algorithm.

the controlled examination time frame, the stroke evolution pace, and the stroke space-concentrated nature. Hence, we deal with a weak field perturbation determined by the dielectric contrast and the spatial distribution, being reasonable to linearize the scattering phenomena by adopting the distorted Born approximation [24]. In this situation, the electric field produced by the transmitting antennas, interacting with the evolving stroke, can be reliably approximated to a reference one. As a result, the differential scattering matrix, $\Delta S(t_0, t_1)$, obtained by subtracting the scattering parameters measured by the system at two different time instants, t_0 and

t_1, is related to the differential contrast through the following integral equation [25]:

$$\Delta S(t_0, t_1) = -\frac{j\,\omega\,\epsilon_b}{2\,a_p\,a_q} \int_D \mathbf{E}_p^{\text{ref}}(\mathbf{r}) \cdot \mathbf{E}_q^{\text{ref}}(\mathbf{r})\,\Delta\chi\,d\mathbf{r}, \quad (2)$$

where D is the volume of the domain of imaging, j is the imaginary unit, $\omega = 2\pi f$ is the angular frequency, and a_p and a_q are the incoming root-power waves given at the p-th and q-th antenna ports, respectively. The symbol "·" denotes the dot product, and $\mathbf{E}_p^{\text{ref}}$, $\mathbf{E}_q^{\text{ref}}$ are the fields radiated by the p-th and q-th antenna inside the reference scenario, in

which the head is approximated as a homogeneous medium whose permittivity is given by the average complex one of the brain.

When exploiting this model to describe the behavior of the MWI scanner, characterized by N antennas operated at n_f frequency points, the integral equation (2) has to be discretized. In doing so, the first step is to obtain the reference fields, $\mathbf{E}^{\text{ref}}$. To this end, a realistic EM full-wave simulation of the reference scenario is performed using an in-house 3-D Finite Element Method (FEM) solver and computer-aided design (CAD) models [26], [27]. The solver applies the curl-curl formulation for the electric field and Galerkin testing and discretizes the whole domain in a tetrahedral mesh. The metal elements, e.g., within the antenna, are considered perfect electric conductor (PEC) surfaces, and the dielectric sub-volumes, e.g., the head and dielectric parts of the antenna, are modeled with the respective complex permittivity. Moreover, the antenna feeding, which is a crucial part to accurately calculate the scattering parameters, is modeled as a section of a rigid coaxial cable (refer to [26] for details). Then, the reference multi-frequency E-fields are interpolated into a 3-mm side Cartesian mesh placed around the upper part of the head consisting of N_c voxels. Finally, (2) is turned into the matrix equation:

$$\Delta S = \mathcal{L}\{\Delta\chi\}, \tag{3}$$

where $\mathcal{L}$ is a $(N \cdot N \cdot n_f) \times N_c$ matrix representing the discretized counterpart of the integral operator in (2), ΔS and $\Delta\chi$ are column vectors having $(N \cdot N \cdot n_f)$ and N_c elements, respectively.

Due to the underlying ill-posedness of the linear inverse problem, $\mathcal{L}$ is ill-conditioned and its direct inversion is not possible. Accordingly, (3) can be solved in a regularized form by adopting the truncated singular value decomposition (TSVD) algorithm [28] as:

$$\Delta\chi = \sum_{n=1}^{L_t} \frac{1}{\sigma_n} \langle \Delta S, u_n \rangle v_n, \tag{4}$$

where σ_n, u_n and v_n are the n-th singular value, right and left singular vectors, respectively, obtained via the singular value decomposition (SVD) of the discretized operator $\mathcal{L}$. In (4), the truncation index L_t acts as a regularizer [28], which is set here to $-30\,\text{dB}$. Here it is worth mentioning that the singular system is computed off-line, while the contrast retrieval, i.e., the inversion, is done real-time, taking a few seconds on a normal laptop. However, the inversion in (4) can be also approached using sparsity-promoting regularization schemes as in [29], [30].

B. PRE-IMAGING

In the experiments, ΔS is obtained by subtracting the $(N \cdot N \cdot n_f)$ S-parameters column vectors measured at two different time instants, t_0 and t_1. Before the ΔS generation, the S-parameters are de-embedded to retrieve their amplitude and phase at the antenna ports. The measured amplitude is

reduced and the phase shifted due to the paths through the switching matrix and the cables that connect the VNA ports to the receiving/transmitting (RX/TX) antennas, as shown in the system diagram in Fig. 1. Thus, each channel (i.e., coaxial cables and switches) is first characterized off-line, and, then, the amplitude reduction and phase shift are removed via de-embedding [31].

In particular, we follow the procedure reported in [22], where, for each pq-antenna pair, the measured scattering matrix at the VNA ports, S^{pq}, includes the scattering matrix of the left path (from the VNA port to p-antenna port), S_L^p, the scattering matrix at the antenna ports, S_{DUT}^{pq}, and the scattering matrix of the right path (from the q-antenna port to the VNA port), S_R^q. Considering the corresponding transmission matrices, T^{pq}, T_L^p, T_{DUT}^{pq}, and T_R^q, respectively, the following represents their relationship:

$$T^{pq} = T_L^p\, T_{\text{DUT}}^{pq}\, T_R^q. \tag{5}$$

Thus the T_{DUT}^{pq} can be retrieved as

$$T_{\text{DUT}}^{pq} = \left(T_L^p\right)^{-1} T^{pq} \left(T_R^q\right)^{-1}, \tag{6}$$

and, finally, rewritten as a scattering matrix, S_{DUT}^{pq}, whose amplitude and phase are now compensated. The de-embedding stage is essential to recover the real and imaginary parts of the dielectric contrast, which is required to characterize the dynamic behavior of the stroke as described in the following section.

C. IMAGE FORMATION

Since we are dealing with a reciprocal network, the differential scattering matrix is expected to be symmetric. However, due to inaccuracies and presence of measurement noise, this ideal condition is not verified in practice. To overcome this issue, the measured differential scattering matrix at each frequency is split into its upper and lower triangular counterparts, which are then rearranged into two $[N \cdot (N-1)/2 \cdot n_f]$ column vectors, say ΔS_u and ΔS_l. Then, ΔS_u and ΔS_l are separately fed into (4) and processed to obtain two contrast estimates, say $\Delta\chi_u$ and $\Delta\chi_l$. Finally, low-pass filtering is applied to both recovered images to remove the outliers from the mapping, which could hide information of interest.

After the low-pass filtering, the two partial maps are fused into a single image where artifacts are expected to be removed or minimized. In fact, in the ideal case of a symmetric differential S-matrix, the information contained in either the upper or lower parts is the same and the retrieved images must be identical within the linear inversion framework herein adopted. This does not hold true in real-life experimentation, where $\Delta\chi_u$ and $\Delta\chi_l$ will be actually different. However, the random sources of errors have a different effect on the two maps, so fusing them allow removing the artifacts.

This procedure, named artifact removal algorithm in Fig. 3, is made in two steps. First, an average image of

the complex differential contrast is formed as:

$$\overline{\Delta}\chi = \frac{1}{2}\sum_{\beta=u,l}\Delta\chi_\beta, \qquad (7)$$

Then, this image is weighted by a normalized mask resulting from the intersection of the normalized upper and lower images:

$$\overline{\overline{\Delta}}\chi = \overline{\Delta}\chi \prod_{\beta=u,l}\widetilde{\Delta}\chi_\beta \qquad (8)$$

where

$$\widetilde{\Delta}\chi_\beta = \frac{|\Delta\chi_\beta|}{max(|\overline{\Delta}\chi|)}. \qquad (9)$$

The map resulting from (8) allows appraising the shape and location of the contrast variation. However, the *direction* of the change which is occurring cannot be directly determined from the normalized mapping. In other words, one cannot distinguish the case of a growing stroke from the case of a regressing stroke. To deal with this issue, we recall the dielectric contrast definition in (1), noticing that the sign of $Re(\overline{\overline{\Delta}}\chi)$ depends on two factors during brain stroke monitoring: first, the stroke status at t_0 and t_1, and, second, the type of stroke. For the former, the sign is the opposite between growing cases and shrinking situations. While, for the latter, the contrast between the stroke-affected area and its healthy surrounding defines the sign. Hence, a HEM case presents a positive sign since the hemorrhagic zone has a higher permittivity than the healthy tissues nearby, either gray or white matter. Conversely, IS shows a negative sign. Therefore, if one already knows the stroke type at the moment of starting the monitoring, which is highly probable in a follow-up situation when a preliminary diagnosis is usually already performed, the unknowns determining the evolution direction reduces to one.

Then, adopting a positive convention to indicate the stroke spreading and a negative, when reducing, we can determine this pathological parameter as

$$\phi = st \frac{Re\left(\overline{\overline{\Delta}}\chi\right)}{\left|max\left(Re\left(\overline{\overline{\Delta}}\chi\right)\right)\right|}, \qquad (10)$$

where st takes the value of 1 in the hemorrhagic case, and -1 in the ischemic case.

IV. EXPERIMENTAL VALIDATION

Aiming to verify the MWI system performance and assess its capabilities of tracking the pathology stage, we consider different stroke stages for both HEM and IS conditions. This section describes the experimental setup and the procedures followed during the experiment and then analyses the results for different monitoring scenarios.
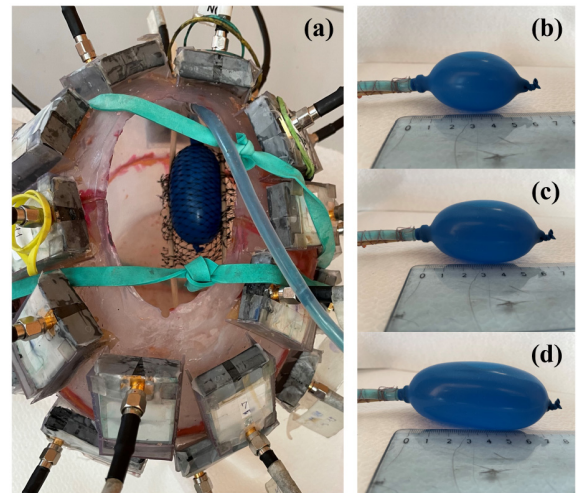

FIGURE 4. Experimental setup and evolving stroke phantom. (a) Top view of the system; (b, c, d) $20\,cm^3$, $40\,cm^3$ and $60\,cm^3$ stroke, respectively.

A. HEAD AND NON-STATIC STROKE PHANTOMS

To validate the imaging system in presence of a brain stroke, it is used a controlled scenario realized through the head and stroke phantoms as depicted in Fig. 4. The set-up is essentially composed of a static part, emulating the steady surrounding tissues, and a dynamic one, i.e., the affected area varying during the measurement.

An anthropomorphic phantom is used for the head, taking as reference the one in [18]. It consists of a single-cavity 3 mm-thick container obtained through 3-D printing in clear resin (polyester casting resin), with antenna supports added externally to facilitate accurate positioning of the array. The phantom was filled with an alcohol-water mixture, with a small percentage of NaCl to increase the conductivity, reaching the average dielectric properties of brain tissues (considering a compound of 75% of white matter and 25% of grey matter) [32]. The liquid was realized in conformity with the standard recipes for SAR measurements reported in [33], refining alcohol-based recipes to obtain a customized formula with commercial 90% ethyl alcohol.

To emulate a stroke, it is employed a capsule-shaped balloon, which can mainly expand in the longitudinal direction, allowing a more accurate assessment of the differences between different scenarios. Then, it is realized a simple support to fix the capsule in the decided position and avoid undesired movements during the experiments. It is well known that different types of strokes exhibit distinct dielectric properties in the microwave frequency spectrum [34]–[36]. The HEM tissue has higher permittivity and conductivity with respect to the surrounding brain tissue, while the IS one has lower values and gives lower contrast. Hence, the target is filled/emptied via a tube-syringe system, with water-alcohol-NaCl mixtures achieving the properties of HEM or IS stroke [35], [36]. All the recipes obtained for the employed liquid mixtures are reported in Table 1, together with the corresponding dielectric parameters at 1 GHz (i.e., relative permittivity, ϵ_r, and conductivity, σ [S/m]). Figure 5
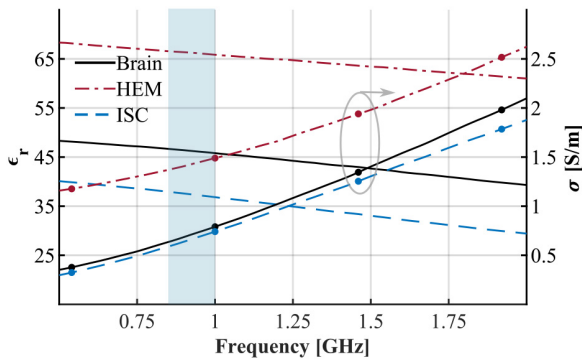
FIGURE 5. Relative permittivity (left axis, lines without markers) and conductivity (right axis, marked lines) of the liquid mixtures mimicking the average brain tissues, the hemorrhagic stroke, and the ischemic stroke. The blue band includes the selected working frequencies.

gives the properties of the liquids measured through the Keysight dielectric probe 85070D and the Keysight N1500A materials measurement software suite [37], in the band 0.5-2 GHz which includes the working frequencies (blue stripe in Fig. 5). Experimental tests demonstrated sufficient stability of the liquids dielectric characteristics considering the time required for the experiment.

B. EXPERIMENTAL PROCEDURE

The laboratory tests were planned to emulate different evolving stages of a brain stroke, considering both the growing and shrinking conditions. In the literature, the documented cases of stroke range from 2 to 200 cm^3 depending on different variables, e.g., time from the diagnosis and location. Further, since continuous monitoring in the early stage through image-based diagnostic is not a common clinical practice, there is no full information about the stroke evolution during the acute phase, while it is known that the stroke can still evolve after 72h after the onset [38]–[41]. On these grounds, the authors tested different stroke dimensions, up to a maximum volume of 60 cm^3.

The experiment consists of differential sets of measurements of a gradually changing scenario, in which, during each set, starting from the empty condition, the target was sequentially filled by adding 20 cm^3 of the stroke-emulating liquid via a tube-syringe system until the worst case, i.e., the largest stroke, has been achieved. Each considered variation corresponds to about 1.5 cm extension in the longitudinal direction (sagittal axes of the human head), that is the range of the estimated resolution (about 1 cm) of the realized MWI scanner [26]. Conversely, the same volumes were repeated voiding the balloon, representing stroke shrinkage. An equivalent procedure was performed for both the IS and HEM cases. Moreover, as aforementioned, each set of measurements takes around 6 min and includes frequency samples at 0.8, 0.85, 0.9, 0.95, and 1 GHz.

The collected data were given in input to the imaging algorithm as multi-frequency differential scattering matrices, in order to reconstruct the scenario at different stages/locations, as detailed in Section III. In the following we consider the
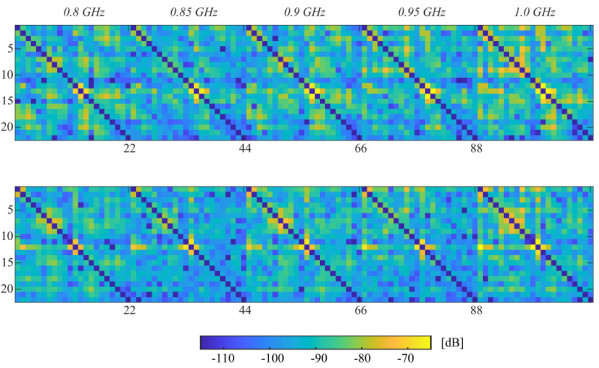

FIGURE 6. Multi-freq differential scattering matrices for 0 to 20 cm^3 volume variation. (Top) Hemorrhagic case; (Bottom) Ischemic case.

differential scenarios between 0 and 20 cm^3, 20 and 40 cm^3, and 40 and 60 cm^3. For instance, Fig. 6 shows the 22 × 22 differential scattering matrices, at the 5 used frequencies, obtained with a 0 to 20 cm^3 case for the HEM and IS types (top and bottom, respectively). It may be noted that the diagonal values, i.e., the reflection coefficients, are forced to zero to underline the range of variation of the transmissions between the antenna pairs, which is the information provided to the imaging algorithm. The data are approximately symmetric, which confirms the reciprocity of the system, comprising expected slight variations due to unavoidable inaccuracies in the measured electrical path, that are compensated via the procedure in Section III.III-C. Furthermore, pointing out the color-map values, all the data in both cases are well above −120 dB, that is the VNA noise floor, at 1 GHz and with an IF filter of 100 Hz [21].

C. RESULTS AND DISCUSSION

As mentioned in Section III, the retrieved contrast map can be normalized using its amplitude, indicating location and shape of the stroke variation, or normalized using its real part and the stroke typology, indicating the changing direction. In this section, we apply both approaches, considering first the localization and shape estimation issue, and then the changing tracking.

1) STROKE LOCALIZATION AND SHAPE ESTIMATION

Once classified the stroke, which is assumed to be done at the patient's admission, the location and shape estimation of the variation of the lesion is vital for the clinical treatment. We approach this medical need using the normalized retrieved dielectric contrast 3-D map (9) as shown in Figs. 7 and 8, for the HEM and IS cases, respectively. Columns I, II, and III indicate the cases 0-20 cm^3, 20-40 cm^3, 40-60 cm^3, respectively.

For the HEM case, Fig. 7 reports the three orthogonal slices through the stroke region center, i.e., sagittal, frontal, and transverse views. For clarity, we add reference dashed lines indicating the approximate position and shape during the experiment of the inflating balloon. From the image it can be noticed that an estimation of the shape can be reached using the values are above −3 dB, yellow zone
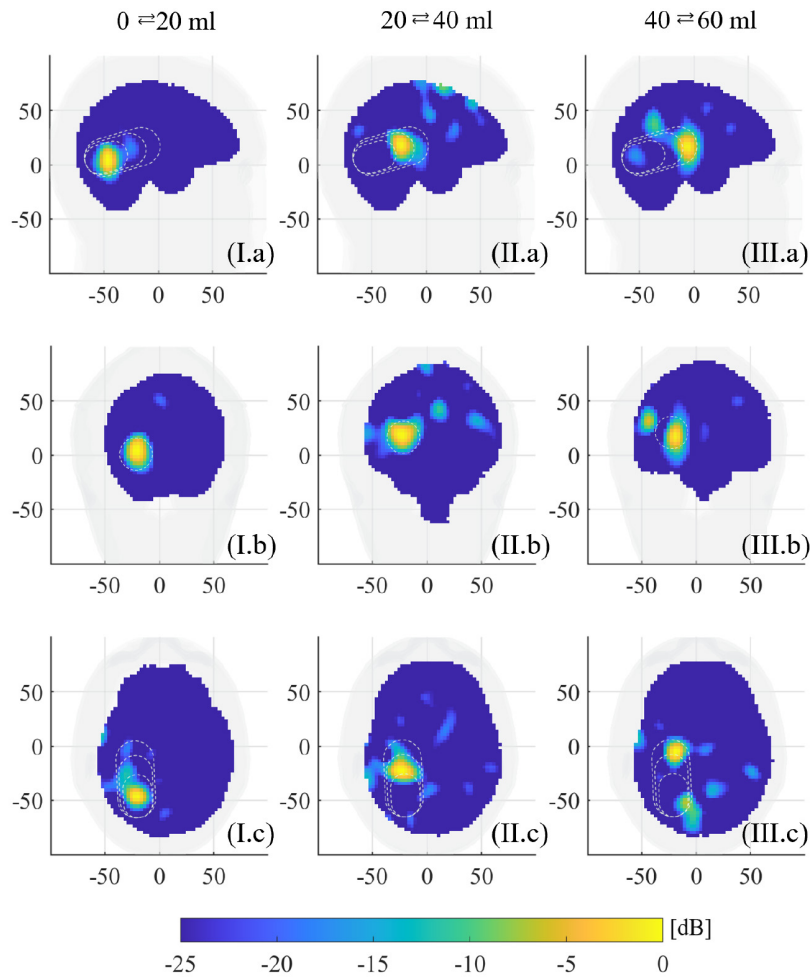
FIGURE 7. Monitoring of HEM progression. Normalized reconstructed dielectric contrast sliced in the middle of the stroke region. (I) Case 0 (healthy) - 20 cm^3; (II) Case 20 - 40 cm^3; (III) Case 40 - 60 cm^3. (a) Sagittal view; (b) frontal view; (c) transverse view.
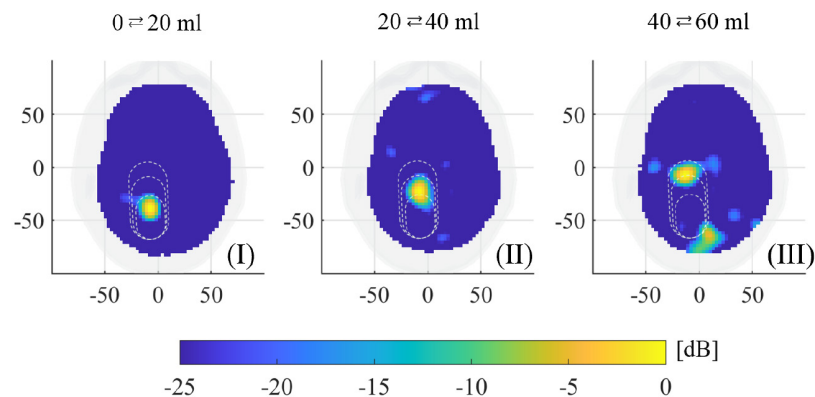

FIGURE 8. Monitoring of IS progression, transverse view. Normalized reconstructed dielectric contrast sliced in the middle of the stroke region. (I) Case 0 (healthy) - 20 cm^3; (II) Case 20 - 40 cm^3; (III) Case 40 - 60 cm^3.

in the figure. For the IS case, in Fig. 8, we just report the transverse view, since is the most significant, and the others views behave similarly to the HEM case. From Figs. 7 and 8, it can be noticed that, first, the imaging algorithm with artifacts removal is clearly able to localize and distinguish the stroke variation, and, second, gives an indication of the

shape of the change for both the studied cases, demonstrating its monitoring capabilities.

In order to verify the repeatability of the measurements, the data collected at different times in the same scenario have been compared. Figures 9 (I.a, I.b) present the differential scattering matrices for two HEM cases changing the
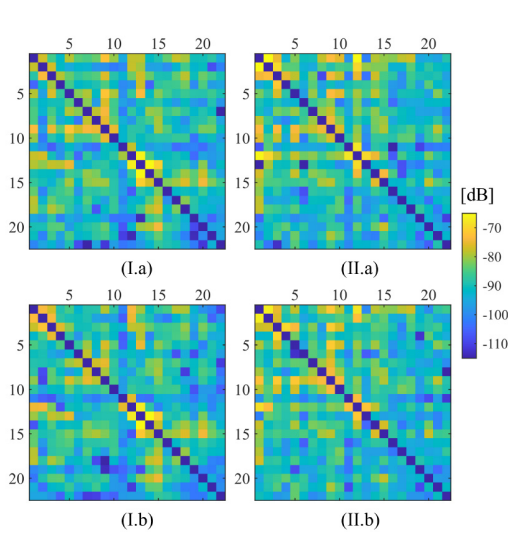
FIGURE 9. Repeatability study: differential scattering matrices for the HEM case. (I.a, I.b) Distinct measurements of equivalent variations 0 to 20 cm^3 at 1GHz; (II.a, II.b) distinct measurements of equivalent variations 20 to 40 cm^3 at 1 GHz.
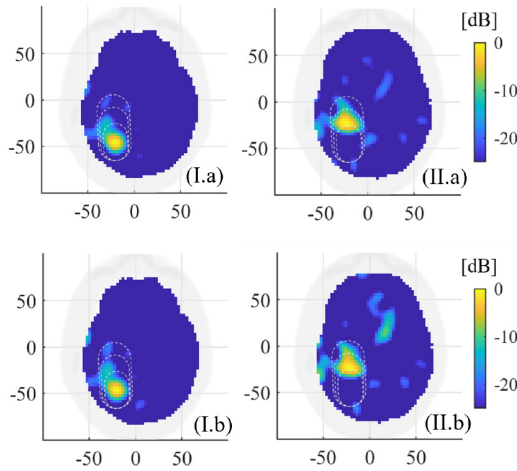

FIGURE 10. Repeatability study: normalized reconstructed dielectric contrast for the HEM case. (I.a, I.b) Images from distinct measurements of equivalent variations 0 to 20 cm^3 at 1GHz; (II.a, II.b) images from distinct measurements of equivalent variations 20 to 40 cm^3.

measured data from 0 to 20 cm^3, while Figs. 9 (II.a, II.b) refer to the case from 20 to 40 cm^3. In both cases, the reached matrix patterns are coherent between the same cases. Then, using the mentioned differential data as input, we reconstruct their respective contrast maps, obtaining very similar counterpart responses, as shown in Fig. 10.

Moreover, the system has been tested against the occurrence of false positives. For this purpose, the data gathered from the same scenario measured at different times were differentiated and used as the input scattering matrix for the algorithm. Figure 11 depicts the differential scattering matrices considering the 20 cm^3 and 40 cm^3 HEM strokes at 1 GHz, and Fig. 12 shows the corresponding retrieved contrasts, normalized with respect to the maximum contrast value of the HEM cases of Fig. 7. It can be noticed that the reconstructed values are always lower than −20 dB.
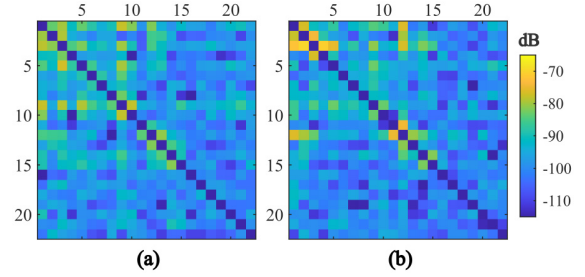

FIGURE 11. False positive test: differential scattering matrices between two different measurements of the same HEM scenario at 1 GHz. (a) 20 cm^3 stroke; (b) 40 cm^3 stroke.
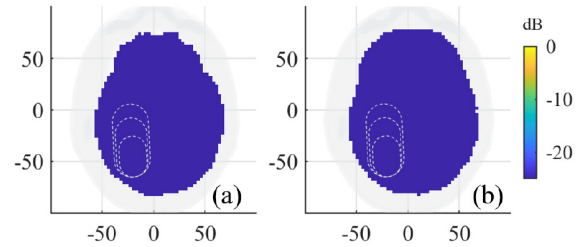

FIGURE 12. False positive test: reconstructed dielectric contrast between two different measurements of the same HEM scenario. (a) 20 cm^3 stroke; (b) 40 cm^3 stroke. The values are normalized with respect to the maximum contrast value as in Fig. 7.

2) STROKE TRACKING

Considering a priori information on the stroke type, the measured data were used to track the pathology shrinking/enlargement, based on the real part of the dielectric contrast map. Knowing the initial sign of the real contrast, the two scenarios can be distinguished by opposite signs of the variations detected in the image. Then, applying this concept by using (10), we can indicate an enlargement with values tending to 1 and a shrink with values close to −1. Figure 13 shows the results considering HEM and IS conditions (case I and II, respectively). The upper row plots are examples of worsening situations when the stroke-affected area is growing: (I.a, II.a) from 0 to 20 cm^3, (I.c) from 20 to 40 cm^3, and (II.c) from 40 to 60 cm^3. On the contrary, the bottom figures are obtained while the stroke is receding: (I.b, II.b) from 20 to 0 cm^3, (I.d) from 40 to 20 cm^3, and (II.d) from 60 to 40 cm^3. It can be noticed that the adopted convention gives positive reconstruction (orange in Fig. 13) where the stroke has spread and negative values (light blue in Fig. 13) where it has retired. Concerning the artifacts aroused in the back of the brain, especially in the IS case, a realistic hypothesis is that it is due to the presence of the tube feeding the balloon, which could undergo undesired movements.

V. CONCLUSION AND FUTURE WORK

The presented work assessed a novel low-complexity scanner for brain stroke imaging dedicated to real-time pathology monitoring during the post-event treatment path. With the first generation prototype as a starting point [18], this contribution presented, first, an innovative antenna array, whose design was improved to meet portability and wearable
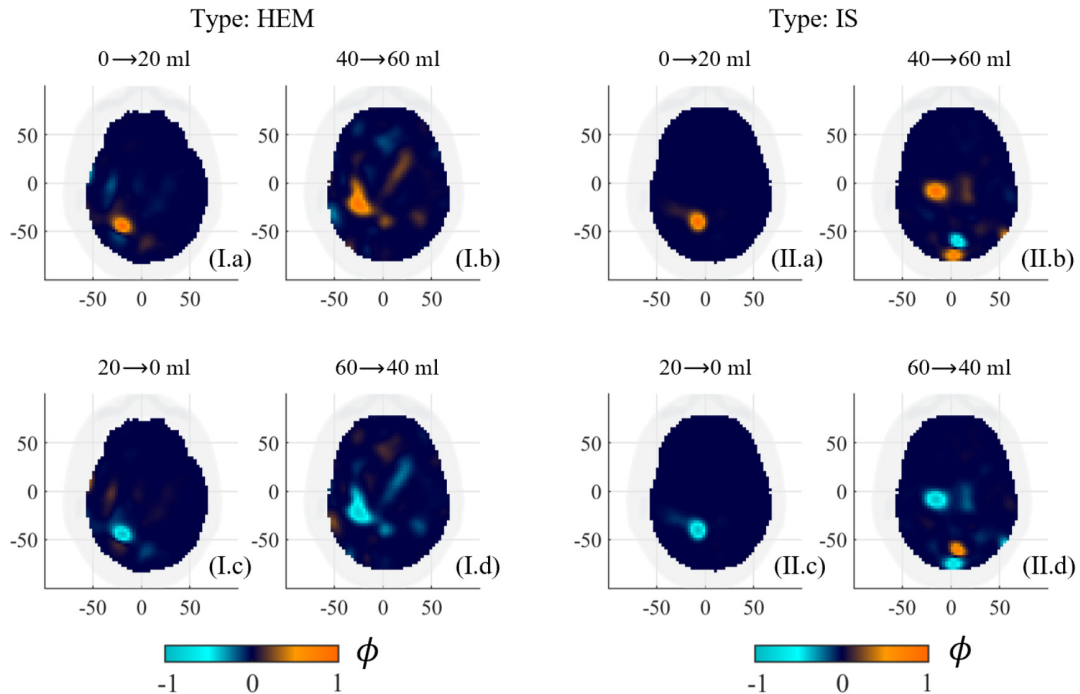
Type: HEM

0→20 ml

40→60 ml

Type: IS

0→20 ml

40→60 ml

(I.a) (I.b) (II.a) (II.b)

20→0 ml 60→40 ml 20→0 ml 60→40 ml

(I.c) (I.d) (II.c) (II.d)

ϕ ϕ

FIGURE 13. Recovering tracking parameters: (I) HEM case; (II) IS case. Growth of the affected area corresponds to positive dielectric contrast (a, b), on the contrary, changes from larger volumes to smaller ones give negative sign (c, d).

requirements. Second, a dynamic phantom was employed to emulate stroke evolution over time, and third, an imaging algorithm, integrated with artifact removal procedures, was able to provide low noise dielectric contrast reconstructions.

The experimental outcomes demonstrated the reliability of the system in localizing the variation of the stroke-affected area with a sensitivity of about 1 cm, comparable with the theoretical resolution. Moreover, it allows the assessment of the disease progress, namely if there is growth or shrinkage between following exams, of great interest for clinical practice.

To further validate the prototype system, the next steps involve the engagement of multi-tissue head phantoms [42] that is not trivial, aiming to incorporate static and non-static components. In addition, substituting actual electromechanical switches with solid-state ones will improve the device performance by decreasing acquisition times by more than 10x, reaching scan times in the order of seconds [16]. Moreover, we plan to further enhance the resolution of the imaging using physics-assisted deep learning algorithms as in [43]. Finally, the authors will investigate novel calibration techniques, such as the one presented in [44], in order to improve the match between the real data and the EM numerical model; in fact, it is well known that any difference between them may affect the imaging operator reliability, thus the image quality.

REFERENCES
[1] E. J. Benjamin *et al.*, "Heart disease and stroke statistics—2019 update: A report from the american heart association," *Circulation*, vol. 139, no. 10, pp. e56–e528, 2019.
[2] R. A. Felberg and A. Naidech, "The five PS of acute ischemic stroke treatment: Parenchyma, pipes, perfusion, penumbra, and prevention of complications," *Ochsner J.*, vol. 5, no. 1, pp. 5–11, 2003.
[3] A. Fhager, S. Candefjord, M. Elam, and M. Persson, "Microwave diagnostics ahead: Saving time and the lives of trauma and stroke patients," *IEEE Microw. Mag.*, vol. 19, no. 3, pp. 78–90, May 2018.
[4] A. Kiourti *et al.*, "Next-generation healthcare: Enabling technologies for emerging bioelectromagnetics applications," *IEEE Open J. Antennas Propag.*, vol. 3, pp. 363–390, 2022.
[5] M. Salucci, A. Polo, and J. Vrba, "Multi-step learning-by-examples strategy for real-time brain stroke microwave scattering data inversion," *Electronics*, vol. 10, no. 1, p. 95, 2021.
[6] M. Persson *et al.*, "Microwave-based stroke diagnosis making global prehospital thrombolytic treatment possible," *IEEE Trans. Biomed. Eng.*, vol. 61, no. 11, pp. 2806–2817, Nov. 2014.
[7] O. Karadima, P. Lu, I. Sotiriou, and P. Kosmas, "Experimental validation of the DBIM-TwIST algorithm for brain stroke detection and differentiation using a multi-layered anatomically complex head phantom," *IEEE Open J. Antennas Propag.*, vol. 3, pp. 274–286, 2022.
[8] I. Bisio *et al.*, "Variable-exponent Lebesgue-space inversion for brain stroke microwave imaging," *IEEE Trans. Microw. Theory Techn.*, vol. 68, no. 5, pp. 1882–1895, May 2020.
[9] A. Fedeli, C. Estatico, M. Pastorino, and A. Randazzo, "Microwave detection of brain injuries by means of a hybrid imaging method," *IEEE Open J. Antennas Propag.*, vol. 1, pp. 513–523, 2020.
[10] M. Hopfer, R. Planas, A. Hamidipour, T. Henriksson, and S. Semenov, "Electromagnetic tomography for detection, differentiation, and monitoring of brain stroke: A virtual data and human head phantom study," *IEEE Antennas Propag. Mag.*, vol. 59, no. 5, pp. 86–97, Oct. 2017.

[11] P.-H. Tournier *et al.*, "Numerical modeling and high-speed parallel computing: New perspectives on tomographic microwave imaging for brain stroke detection and monitoring," *IEEE Antennas Propag. Mag.*, vol. 59, no. 5, pp. 98–110, Oct. 2017.

[12] A. Brankovic *et al.*, "Unsupervised algorithm for brain anomalies localization in electromagnetic imaging," *IEEE Trans. Comput. Imag.*, vol. 6, pp. 1595–1606, Dec. 2020.

[13] A. S. M. Alqadami, N. Nguyen-Trong, B. Mohammed, A. E. Stancombe, M. T. Heitzmann, and A. Abbosh, "Compact unidirectional conformal antenna based on flexible high-permittivity custom-made substrate for wearable wideband electromagnetic head imaging system," *IEEE Trans. Antennas Propag.*, vol. 68, no. 1, pp. 183–194, Jan. 2020.

[14] A. S. M. Alqadami, A. Zamani, A. Trakic, and A. Abbosh, "Flexible electromagnetic cap for three-dimensional electromagnetic head imaging," *IEEE Trans. Biomed. Eng.*, vol. 68, no. 9, pp. 2880–2891, Sep. 2021.

[15] D. Tajik, R. Kazemivala, and N. K. Nikolova, "Real-time imaging with simultaneous use of born and Rytov approximations in quantitative microwave holography," *IEEE Trans. Microw. Theory Techn.*, vol. 70, no. 3, pp. 1896–1909, Mar. 2022.

[16] M. Haynes, J. Stang, and M. Moghaddam, "Real-time microwave imaging of differential temperature for thermal therapy monitoring," *IEEE Trans. Biomed. Eng.*, vol. 61, no. 6, pp. 1787–1797, Jun. 2014.

[17] M. Wang, R. Scapaticci, M. Cavagnaro, and L. Crocco, "Towards a microwave imaging system for continuous monitoring of liver tumor ablation: Design and in silico validation of an experimental setup," *Diagnostics*, vol. 11, no. 5, p. 866, 2021.

[18] D. O. Rodriguez-Duarte *et al.*, "Experimental validation of a microwave system for brain stroke 3-D imaging," *Diagnostics*, vol. 11, no. 7, p. 1232, 2021.

[19] R. Scapaticci, J. Tobon, G. Bellizzi, F. Vipiana, and L. Crocco, "Design and numerical characterization of a low-complexity microwave device for brain stroke monitoring," *IEEE Trans. Antennas Propag.*, vol. 66, no. 12, pp. 7328–7338, Dec. 2018.

[20] D. O. Rodriguez-Duarte, S. de Luque Arias, J. A. T. Vasquez, R. Scapaticci, L. Crocco, and F. Vipiana, "A portable microwave scanner for brain stroke monitoring: Design, implementation and experimental validation," in *Proc. 16th Eur. Conf. Antennas Propag. (EuCAP)*, 2022, pp. 1–5.

[21] "Keysight streamline series USB vector network analyzer P937XA 2-port, up to 26.5 GHz," Data Sheet, Keysight Technol., Santa Rosa, CA, USA, 2018.

[22] J. A. T. Vasquez *et al.*, "Design and experimental assessment of a 2D microwave imaging system for brain stroke monitoring," *Int. J. Antennas Propag.*, vol. 2019, May 2019, Art. no. 8065036.

[23] D. O. Rodriguez-Duarte, J. A. T. Vasquez, R. Scapaticci, L. Crocco, and F. Vipiana, "Brick-shaped antenna module for microwave brain imaging systems," *IEEE Antennas Wireless Propag. Lett.*, vol. 19, no. 12, pp. 2057–2061, Dec. 2020.

[24] M. Pastorino, *Imaging Configurations and Model Approximations*. Hoboken, NJ, USA: Wiley, 2010, ch. 4, pp. 57–78.

[25] N. K. Nikolova, *Introduction to Microwave Imaging*. Cambridge, U.K.: Cambridge Univ. Press, 2017.

[26] D. O. Rodriguez-Duarte, J. A. T. Vasquez, R. Scapaticci, L. Crocco, and F. Vipiana, "Assessing a microwave imaging system for brain stroke monitoring via high fidelity numerical modelling," *IEEE J. Electromagn., RF, Microw. Med. Biol.*, vol. 5, no. 3, pp. 238–245, Sep. 2021.

[27] E. A. Attardo, A. Borsic, G. Vecchi, and P. M. Meaney, "Whole-system electromagnetic modeling for microwave tomography," *IEEE Antennas Wireless Propag. Lett.*, vol. 11, pp. 1618–1621, Dec. 2012.

[28] M. Bertero and P. Boccacci, *Introduction to Inverse Problems in Imaging*. Boca Raton, FL, USA: CRC Press, 1998.

[29] G. Oliveri, M. Salucci, N. Anselmi, and A. Massa, "Compressive sensing as applied to inverse problems for imaging: Theory, applications, current trends, and open challenges," *IEEE Antennas Propag. Mag.*, vol. 59, no. 5, pp. 34–46, Oct. 2017.

[30] N. Vojnovic, L. Crocco, and M. N. Stevanovic, "A three-dimensional microwave sparse imaging approach using higher-order basis functions," *Int. J. Antennas Propag.*, vol. 2022, Mar. 2022, Art. no. 1839842.

[31] "De-embedding and embedding S-parameter networks using a vector network analyzer," Application Notes, Keysight Technol., Santa Rosa, CA, USA, 2020.

[32] N. Joachimowicz, B. Duchêne, C. Conessa, and O. Meyer, "Anthropomorphic breast and head phantoms for microwave imaging," *Diagnostics*, vol. 8, no. 4, p. 85, 2018.

[33] *IEEE Recommended Practice for Determining the Peak Spatial-Average Specific Absorption Rate (SAR) in the Human Head From Wireless Communications Devices: Measurement Techniques*, IEEE Standard 1528-2013 (Revision IEEE Std 1528-2003), 2013.

[34] S. Semenov, T. Huynh, T. Williams, B. Nicholson, and A. Vasilenko, "Dielectric properties of brain tissue at 1 GHz in acute ischemic stroke: Experimental study on swine: Dielectric properties of brain tissue in acute stroke," *Bioelectromagnetics*, vol. 38, no. 2, pp. 158–163, 2017.

[35] S. Y. Semenov and D. R. Corfield, "Microwave tomography for brain imaging: Feasibility assessment for stroke detection," *Int. J. Antennas Propag.*, vol. 2008, pp. 1–8, May 2008.

[36] D. Ireland and M. Bialkowski, "Feasibility study on microwave stroke detection using a realistic phantom and the FDTD method," in *Proc. Asia-Pacific Microw. Conf.*, 2010, pp. 1360–1363.

[37] "N1500A Materials Measurement Suite." 2022. [Online]. Available: https://www.keysight.com/it/en/product/N1500A/materials-measurement-suite.html

[38] C. Laredo *et al.*, "Prognostic significance of infarct size and location: The case of insular stroke," *Sci. Rep.*, vol. 8, p. 9498, Jun. 2018.

[39] A. Bruno, N. Shah, A. E. Akinwuntan, B. Close, and J. A. Switzer, "Stroke size correlates with functional outcome on the simplified modified rankin scale questionnaire," *J. Stroke Cerebrovasc. Dis.*, vol. 22, no. 6, pp. 781–783, 2013.

[40] J. L. Saver, "Time is brain-quantified," *Stroke*, vol. 37, no. 1, pp. 263–266, 2006.

[41] J. L. Saver *et al.*, "Infarct volume as a surrogate or auxiliary outcome measure in ischemic stroke clinical trials," *Stroke*, vol. 30, no. 2, pp. 293–298, 1999.

[42] G. Ruvio *et al.*, "Multimodal breast phantoms for microwave, ultrasound, mammography, magnetic resonance and computed tomography imaging," *Sensors*, vol. 20, no. 8, p. 2400, 2020.

[43] A. Y. Ruiz, M. Cavagnaro, and L. Crocco, "A physics-assisted deep learning microwave imaging framework for real-time shape reconstruction of unknown targets," *IEEE Trans. Antennas Propag.*, early access, Apr. 5, 2022, doi: 10.1109/TAP.2022.3162320.

[44] C. Origlia, D. O. Rodriguez-Duarte, J. A. T. Vasquez, and F. Vipiana, "Microwave antenna array calibration via simulated and measured S-parameters matching," in *Proc. 16th Eur. Conf. Antennas Propag. (EuCAP)*, 2022, pp. 1–4.

DAVID O. RODRIGUEZ-DUARTE (Graduate Student Member, IEEE) received the B.Sc. and M.Sc. degrees in electronic engineering from the Universidad Nacional de Colombia in 2013 and 2018, respectively, and the Ph.D. degree *(summa cum laude)* Politecnico di Torino, Italy, in 2022, where he is a Research Fellow with the Department of Electronics and Telecommunications. He is currently involved in Designing Microwave Imaging Systems with the Applied Electromagnetics Group. He has been a Marie Sklodowska-Curie Early-Stage-Research Fellow as part of the European Project EMERALD, being Visiting Research in WIPL-D, Serbia, iLumens-Health Simulation Center, France, and Keysight, France. In 2015, he collaborated with the Control and Energy Nanosatellites Group, Universidad Sergio Arboleda, Colombia. In 2017, he was a Visiting Researcher with the University of British Columbia, Kelowna, Canada, funded by the Emerging Leaders in the Americas Program. He has been awarded the Best Undergraduate Thesis of the Electronics Department in 2013, the Second Prize in the Student Paper Competition in the 2021 URSI General Assembly Scientific Symposium, the AP-S Tapan Sarkar Best Student Paper in 2021 IEEE International Conference on Antenna Measurements and Applications, the C. J. Reddy Travel Grant for Graduate Students in IEEE AP-S/URSI 2021, the best Propagation Paper Finalist in the 2022 European Conference on Antennas (EuCAP2022), and the Young Scientist Award with the URSI combined Atlantic/Asia-Pacific Radio Science Conference (AT-AP-RASC) in 2022.

CRISTINA ORIGLIA was born in Mondovì, Italy, in 1996. She received the B.S. degree and the M.S. degree *(summa cum laude)* in biomedical engineering with the thesis focused on the implementation of a calibration technique for microwave antenna arrays from the Politecnico di Torino, Torino, Italy, in 2018 and 2021, respectively, where she is currently pursuing the Ph.D. degree in electrical, electronics and communications engineering. Her research activity is focused on the development of a microwave brain imaging device, including electromagnetic simulation and experimental testing on phantoms. She received the honorable mention "Ingenio al Femminile" from the Italian Council of Engineers, in 2021.

JORGE A. TOBÓN VASQUEZ (Member, IEEE) received the Degree in electronics engineering from the Universidad de Antioquia, Colombia, in 2010, in a double degree program, the master's degree in electronic engineering and the Ph.D. degree in electronics and telecommunication engineering from the Politecnico di Torino, Italy, in 2010 and 2014, respectively, where he is an Assistant Professor. His main research activities correspond to modeling, designing, and analyzing systems for microwave imaging applications, specifically in the biomedical and food industry fields, and the numerical modeling of complex and nonhomogeneous media propagation. He received the "Premio Latmiral," an award granted by the Italian Society of Electromagnetism in 2018 and the URSI General Assembly Scientific Symposium Young Scientist Award and the Sorrentino URSI Italy National Meeting Young Scientist Paper Award in 2020.

ROSA SCAPATICCI (Member, IEEE) was born in Naples, Italy, in 1985. She received the Laurea degree *(summa cum laude)* in biomedical engineering from the "Federico II" University of Naples, Naples, in 2010, and the Ph.D. degree in information engineering from the "Mediterranea" University of Reggio Calabria, Reggio Calabria, Italy, in 2014. From December 2013, she has been working with the Institute of Electromagnetic Sensing of the Environment, National Research Council of Italy, Naples, first as a Research Fellow and from September 2017 as a Researcher. She has coauthored more than 60 papers on international journals and conference proceedings. Her scientific interests include electromagnetic scattering problems, imaging methods for noninvasive diagnostics and they are mainly focused on the development of innovative microwave imaging approaches in the framework of biomedical applications, as well as therapeutic applications of electromagnetic fields. She received the best Student Member Paper Award from the IEEE Antennas and Propagation Society Central and Southern Italy Chapter in 2013 and the Italian Society of Electromagnetics, the Barzilai Award and the Latmiral Award in September 2014 and in September 2018, respectively. In 2021, she received the Associate Professor Habilitation in Electromagnetic fields, by the Italian Ministry of Research and University. She is an Associate Editor of the IEEE TRANSACTIONS ON MEDICAL IMAGING.

LORENZO CROCCO (Senior Member, IEEE) received the Full Professor Habilitation degree in electromagnetic fields from the Italian Ministry of Research and University in 2018. He is a Research Director with the Institute for the Electromagnetic Sensing of the Environment, National Research Council of Italy (IREA-CNR). His scientific activities mainly concern electromagnetic scattering, with a focus on diagnostic and therapeutic uses of EM fields, through-the-wall radar, and GPR. On these topics, he has published more than 120 papers, given keynote talks and lectures, and led or participated to National and International Research Projects. He is an Associate Editor of the IEEE JOURNAL OF ELECTROMAGNETICS, RF AND MICROWAVES IN MEDICINE AND BIOLOGY and has edited a book on *Electromagnetic Technologies for Brain Diseases Diagnostics, Monitoring and Therapy*. From 2013, he is the Italian Representative with the Management Committees of COST Actions devoted to Medical Applications of EM fields (MiMed on microwave imaging and MyWAVE on therapeutic applications of electromagnetic waves). He has been a member of the Board for the European School of Antennas since 2015, the Board of Directors of the Italian Electromagnetic Society (SIEm) since 2017, and the Italian URSI Commission (International Union of Radio Science) since 2019. In 2019, he has been Elected in the Scientific Board of the Engineering Department (DIITET) of CNR. He was a recipient of the SIEm "Barzilai" Award for Young Scientists in 2004 and YSA with the URSI General Assembly, New Delhi, India, in 2005. He is a Fellow of the Electromagnetic Academy (TEA) and a URSI Senior Member.

FRANCESCA VIPIANA (Senior Member, IEEE) received the Laurea and Ph.D. (Dottorato di Ricerca) degrees in electronic engineering from the Politecnico di Torino, Torino, Italy, in 2000 and 2004, respectively, She was a Postdoctoral Research with the European Space Research Technology Center, Noordwijk, The Netherlands. From 2005 to 2008, she was a Research Fellow with the Department of Electronics, Politecnico di Torino. From 2009 to 2012, she was the Head of the Antenna and EMC Laboratory, Istituto Superiore Mario Boella, Torino. Since 2012, she has been an Assistant Professor with the Department of Electronics and Telecommunications, Politecnico di Torino, where she has been an Associate Professor since 2014 and a Full Professor since 2021. She is currently involved in the analysis, synthesis, and optimization of multiband reconfigurable compact antennas, and in the modelling and design of microwave imaging systems, for medical and industrial applications. Her current research interests include numerical techniques based on the integral equation and method of moment approaches, with a focus on multiresolution and hierarchical schemes, domain decomposition, preconditioning and fast solution methods, and advanced quadrature integration schemes. She received the Young Scientist Award with the URSI General Assembly in 2005, the First Prize in the Poster Competition with the IEEE Women in Electromagnetics Workshop in 2009, the ISMB Best Paper Award in 2011, and the Lot Shafai Mid-Career Distinguished Award from the IEEE Antennas and Propagation Society in 2017. She is also on the Editorial Board of the IEEE TRANSACTIONS ON ANTENNAS AND PROPAGATION and *IEEE Antennas and Propagation Magazine*.